

Design, Construction, and Operation of Liquid Nitrogen Cooled MHD Miniature Ship with No-insulation High Temperature Superconductor Magnet

Kyoungmo Koo*, Chaemin Im*, Geonyoung Kim, Jaemin Kim, Seungyong Hahn, and Sangjin Lee

Abstract—A feasibility study of a magnetohydrodynamic (MHD) ship using no-insulation (NI) high-temperature superconductor (HTS) magnets made of rare earth barium cobalt oxide (REBCO) tape is presented. Based on the preliminary design, fabrication, and experimental results of a miniature MHD ship with NI HTS magnets in a liquid nitrogen environment (77 K), a scale-up design of a full-size MHD ship with REBCO NI HTS magnets at 20 K is presented. The final velocity of the miniature MHD ship is measured to be 4.0 cm/s, which represents 41.7% of the theoretically calculated velocity. Since the applicability of REBCO NI HTS magnets to MHD propulsion is confirmed, a scale-up design of their application to Yamato-1, the first MHD ship with low-temperature superconductor magnets (LTS), is presented. The operating parameters when the designed magnets are applied are compared with those of Yamato-1. Based on the same geometry, it is demonstrated that the application of NI HTS magnets at 20 K can improve the central magnetic field and propulsive Lorentz force by about 3 times compared to the Yamato-1 operated at 4 K.

Index Terms—Magnetohydrodynamics, High-temperature superconductors, Large-scale systems, Acceleration measurement, Marine vehicle propulsion

I. INTRODUCTION

THE remarkably low acoustic signature of magnetohydrodynamic (MHD) propulsion systems has rendered them an exceptionally appealing choice for deployment, particularly in submarine applications [1]–[3]. This advanced propulsion technology operates with a level of near-silence, which is of paramount importance in the stealthy domain of undersea operations. Unlike traditional propellers, which produce noise through the mechanical rotation of blades and the turbulent flow of water, MHD propulsion leverages electromagnetic

This work was supported in part by National R&D Program through the National Research Foundation of Korea (NRF) funded by Ministry of Science and ICT (2022M3I9A1073924), in part by National R&D Program through the National Research Foundation of Korea (NRF) funded by Ministry of Science and ICT (2022M3I9A1072846). (*Corresponding author: Seungyong Hahn.*)

K. Koo was with the Department of Electrical and Computer Engineering, Seoul National University. He is now with the Department of Electrical and Computer Engineering, University of Michigan at Ann Arbor, MI 48109, USA.

C. Im, G. Kim, S. Hahn, and S. Lee are with the Department of Electrical and Computer Engineering, Seoul National University, Seoul 08826, Korea (e-mail: hahnsy@snu.ac.kr).

J. Kim is with the Applied Superconductivity Center, Electric Power Research Institute of Seoul National University, Seoul, 08826, Korea.

* Kyoungmo Koo and Chaemin Im contributed equally to this work.

principles to generate thrust without the need for moving parts. By doing so, it minimizes both the sound emissions and the vibrations that could otherwise compromise a submarine's concealment, making MHD propulsion a highly sought-after and advantageous option for modern underwater warfare and exploration. In 1991, D. W. Swallom *et al.* proposed the design of an attack-class submarine that uses MHD technology, using an optimization method [3]. Moreover, the MHD propulsion system has proven effective for pumping materials that pose challenges for conventional pumps, a topic examined in [4]. Additionally, when applied to the marine environment, it provides a solution to structural problems inherent in conventional rotary propellants, such as cavitation issues [5].

Concurrently, the ongoing advancements in superconductivity technology have paved the way for a multitude of research endeavors and investigations that have explored the potential applications of superconductivity within the context of MHD-propelled ships [6]–[12]. Among those studies, however, there are few cases of actual driving except for Yamato-1 in 1992 [13], [14], which was reported by Y. Sasakawa *et al.*, due to the fact that high propulsion efficiency and thrust can be obtained only by generating a high magnetic field. In 2016, an experiment conducted by P. Hales and colleagues involved the use of a high-temperature superconductor (HTS) known as Bismuth Strontium Calcium Copper Oxide (BSCCO) within a solid - nitrogen environment. This unique setup was described by the authors as a "Thermal Battery." However, the quantitative analysis of the actual propulsion system is not fairly provided [15]. Subsequently, in 2017, D. Cébron conducted experiments focused on measuring the propulsion characteristics of an MHD ship. These experiments involved varying the saltwater concentrations and battery voltage conditions. The propulsion system used in this experiment utilized a permanent magnet and a LiPo battery [16]. The aim of these experiments was to better understand how different parameters, such as saltwater concentration and battery voltage, affected the performance of the MHD propulsion system. In this research, the authors asserted that in order to attain a propulsion efficiency comparable to that of a commercial thruster, an MHD thruster necessitates a magnetic field strength of at least 10 Tesla (10 T).

In general, high-temperature superconducting materials are characterized by their ability to exhibit superconductivity at

temperatures above the boiling point of liquid nitrogen, as established in previous studies [17], [18]. These materials exhibit relatively higher critical properties, including temperature, current-carrying capacity, and resistance to magnetic fields when compared to low-temperature superconducting (LTS) materials. These exceptional properties have raised considerable expectations that high-temperature superconductors could bring about a significant breakthrough in the realm of high-field magnets and their diverse applications. One of the notable advantages of high-temperature superconductors lies in their remarkable thermal capacity, which was initially seen as a positive attribute for ensuring stability. This characteristic is particularly valuable in preventing 'quench,' which refers to the inadvertent loss of superconductivity. However, it is essential to acknowledge that this advantage also carries a drawback when it comes to the 'protection' of the magnet. The low thermal diffusivity of these materials causes energy to accumulate in localized areas, which can potentially lead to overheating and the burnout of the magnet, necessitating careful management of this aspect in practical applications.

Following the pioneering introduction of no-insulation (NI) technology in 2011, which intentionally eliminates the insulation of high-temperature superconducting (HTS) magnets [19], multiple studies and experiments of no-insulation magnets have been reported [20]–[26]. Magnets utilizing this technology have achieved successful production of high-magnetic field capabilities [27]–[33], achieving the creation of the world's highest DC magnetic field of 45.5 T using an HTS insert magnet in 2019 [34]. These remarkable results suggest the potential for magnets applied on MHD ships to approach a high magnetic field, all while maintaining operational stability through the utilization of NI HTS technology.

II. DRIVING QUESTIONS & DESIGN PHILOSOPHIES

In general, electromagnetic, thermal, mechanical, and fluid-dynamics factors are considered in electrical device design. The design of the MHD system including superconductor magnets should also consider these aspects. However, mechanical factors are not considered because the magnet used in the experiment of this study has a significantly lower stress level than the critical value. Instead, given the novel connection of a superconductor magnets and battery in series within an MHD system, it is imperative to undertake a thorough circuit analysis of the system. The driving questions that are addressed from these analyses are as follows:

- Electromagnetic: Can the experimental results of REBCO NI HTS magnets match with the simulation data in the MHD system?
- Thermal: Can coolant be maintained over a safe level throughout the experiment despite heat transfer by conduction and convection?
- Fluid-dynamics: How different would the speed of a REBCO applied MHD ship be compared to theoretical calculations based on fluid-dynamics and why?
- Circuit: Can REBCO NI HTS operate safely in a series connection with a battery? Also, what is the optimal capacity of the battery considering the time constant of NI HTS?

The key philosophies of this study are largely fourfold: ignorance of detail, ease of manufacturing, physically measurable parameters, and verification and scale-up.

TABLE I
KEY PARAMETERS OF THE TESTED MINIATURE MHD SHIP

Parameters	Units	Value	
Magnet Parameters		Coil 1	Coil 2
Inner radius	[mm]	30.0	
Outer radius	[mm]	40.7	40.5
Magnet height	[mm]	8.4	
Number of turns per double pancake (DP)		153	150
Inductance	[mH]	2.19	2.12
Characteristic resistance	[$\mu\Omega$]	156	98
Time constant	[s]	14.0	21.6
Operating temperature	[K]	77.0	
Critical current	[A]	80.6	81.2
Coil current	[A]	70.0	
Ship Parameters			
Max. X; Y; Z length	[mm]	300; 208; 181	
Electrode gap	[mm]	48.0	
Total mass	[kg]	3.0	
Saltwater concentration	[%]	30	
Average magnetic field between electrodes	[mT]	54.9	
Saltwater conductivity	[S/m]	22.0	
Applied voltage	[V]	23.0	
Resistance between electrodes	[Ω]	0.4	
Current through electrodes	[A]	70.0	
Lorentz's force	[mN]	184.5	

In the context of the driving questions outlined in the previous paragraph, the design of the MHD ship used in the experiment is separated into three distinct parts: 1) the electromagnetic part, including electrodes and magnets with the potential between electrodes and magnetic fields created by superconducting magnets considered, 2) thermal part including LN₂ container with heat transfer considerations, and 3) the fluid-dynamics part, which encompasses floats with buoyancy considered. Table I shows the key parameters of the overall system of tested miniature MHD ship.

A. Electromagnetic design: Superconducting magnets

As shown in fig. 1, the width and length of the LN₂ container are determined as the value that can contain the Glass Fiber-Reinforced Plastic (GFRP, G10) plate and DP coil with 40% margin, so the width and length of the container are each designed as 18 mm and 150 mm. Each parameter is designed considering that the thickness of the magnet and g10 plate is 13.0 mm, and the length of the g10 plate is 106 mm. The electrodes are positioned such that the center of the magnet and the center of the electrode pair are aligned at the same height, resulting in the maximum magnetic field experienced by the duct space through which seawater flows between them, under ideal inter-electrode gap conditions.

A simulation is conducted using COMSOL Multiphysics® with critical current data of 4 mm superconducting tape

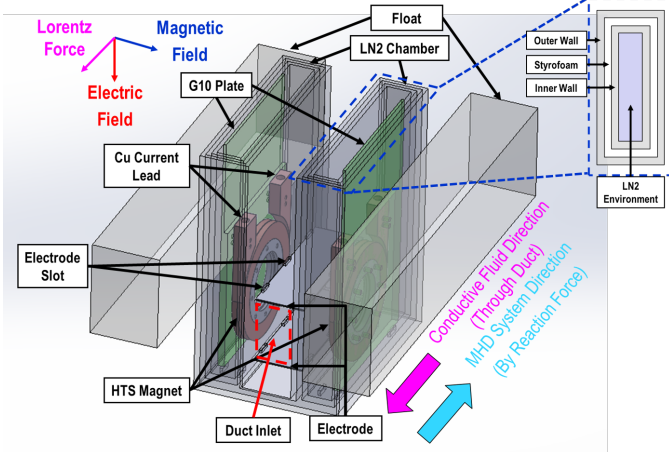


Fig. 1. The figure shows Lorentz's force and overall design of a ship. The magnetic field is created horizontally and the voltage is applied to electrodes, inducing vertical current from the anode to the cathode. Lorentz's force is generated in the direction of the external product of the current and magnetic field. The ship consists of three parts: 1) Styrofoam float (Float); 2) LN₂ container (gray part). Slots, which are 2 mm long, have been placed to fix electrodes between two LN₂ containers.; 3) HTS magnet with g10 plate (green part). The upper right figure is a top view of the LN₂ container. The thickness of the outer wall, inner wall, and Styrofoam is 3 mm each. The total thickness of the wall is 9 mm.

manufactured by SuNAM [35]. The critical current of HTS magnets is expected to be 80.6 A and 81.2 A for each coil.

The average field magnitude between two electrodes is calculated as 54.9 mT. Since the field due to Earth's magnetic field is about 40 μ T in Korea, the effect can be neglected.

TABLE II
COMPARATIVE RESULTS OF CASE STUDIES ON NI HTS MAGNETS

Case	Inner / Outer Diameter (mm)	Critical / Operating Current (A)	Magnetic Field Density (mT)
1	6 / 54	55.0 / 38.5	59
2	60 / 80	80.5 / 56.2	99
3	208 / 214	120 / 84.0	41

The HTS magnets are designed and wound in DP type with 80 m of HTS tape for each pole. The inner diameter (ID) and outer diameter (OD) have been chosen as 60 mm and 84 mm, respectively, based on multiple case studies conducted at 70% of critical current conditions to maximize magnetic field density. The results of case studies are represented in table II.

B. Thermal design: LN₂ containers

As illustrated in fig. 1, to facilitate the supply of liquid nitrogen during the experiment, the upper face of the LN₂ container is designed to be exposed to the air. The parameters of LN₂ containers are determined as follows.

The container wall has a total thickness of 9 mm and must be designed to provide thermal insulation while ensuring structural stability. This has been achieved by sandwiching Styrofoam between two layers of 3D-printed PLA material. Insulating electrodes from the coolant is important to prevent icing around the electrodes. Since the ice is an insulator

with extremely low electrical conductivity, which is less than 10⁻⁹ S/m, even less than 0.1 mm of the ice can completely degrade the ship's overall performance. The Styrofoam part and each PLA wall of each side are designed to be 3 mm each.

The height of the LN₂ container is determined by eq. (1).

$$\dot{Q} = (T_{\infty 1} - T_{\infty 2}) / \frac{L}{kA} + (T_{\infty 1} - T_{\infty 2}) / hS, \quad (1)$$

where $T_{\infty 1}$ (300 K) and $T_{\infty 2}$ (77 K) stand for room temperature and the temperature of LN₂. k stands for the thermal conductivity of the air, L for an air gap, A for the LN₂ container outer area, h for the convection coefficient of the air, and S for the area of the bottom of the LN₂ container. \dot{Q} stands for transferred-heat energy per second. S and \dot{Q} stand for the same parameters for eq. (2).

The evaporation rate, E of LN₂ is calculated as eq. (2). h_l is the latent heat of vaporization of LN₂.

$$E = \frac{\dot{Q}}{S \times h_l}, \quad (2)$$

Based on eq. (1) and (2), the height of container is designed as 172 mm to maintain LN₂ for 400 seconds, considering nonlinearity of evaporation rate.

C. Fluid-dynamics design: Float

As in fig. 1, “floats” made of styrofoam are installed on both sides of a ship to create buoyancy for the body. Since the electrodes should be fully immersed under the saltwater, the lower surfaces of the floats are placed at the same height as the anode (upper electrode). Given the total weight of the boat, 3 kg, and its buoyancy, the required volume of the submerged part is calculated to be 2,307 cm³. The length of the float is determined to be 30 cm to ensure sufficient glide distance for the boat in the test pool with a total length of 1 m. The performance is proportional to the length of floats since the front surface submerged in the seawater (S_{front}) of floats is inversely proportional to its length, as shown in eq. (3). The S_{front} also is proportional to form drag force, which will be further discussed as the main factor of drag force in eq. (7).

$$\frac{m}{\rho} = 2S_{front}L_{float} + V_{thruster}, \quad (3)$$

where m states for the weight of the ship, ρ for the density of saltwater, S_{front} for the immersed frontal space of each float, L_{float} for the length of the float, and $V_{thruster}$ for the immersed volume of the thruster. The immersion depth, which is the distance between the surface of the seawater and the bottom surface of the float, is 2.2 cm, and the height of floats ($d_{immerse}$) is 7 cm, which is more than 3 times of immersion depth to prevent capsizing. The width of the floats is 10 cm.

D. Circuit design: Lumped circuit and time constant

As stated in reference [19], the winding process for NI HTS magnets involves deliberately omitting insulation layers, a departure from conventional HTS magnets. As a result, the

flow of current in NI HTS magnets occurs not only along the circumferential path, but also through the radial path. The radial path lacks superconductivity, causing it to exhibit resistive behavior. This resistance is commonly referred to as the characteristic resistance, denoted as R_c . Since the values of the current through each coil are lower than their critical values, the superconductor resistance, R_{sc} , is negligible. As taking the values of the inductance L of each coil, the equivalent circuit is modeled as fig. 2, including the voltage of the LiPo battery (V), the shunt resistor (R_{shunt}), and overpotential (E_0).

The characteristic resistances and inductances of coil 1 and coil 2 are measured as $156 \mu\Omega$, 2.19 mH and $98 \mu\Omega$, 2.12 mH , respectively. The time constant of each coil is calculated as 14.0 s and 21.6 s . Since the time it takes to reach the 95% level of the target magnetic field is about three times the time constant of the coil, the container is designed to withstand 270 seconds , which is about ten times the time constant. Plus, the optimal capacity of a battery is determined by the time constant and the duration of ship movement, according to the eq. (4). The optimal battery capacity turned out to be 2200 mAh , which is the capacity of the battery used in the experiment.

$$C_{bat} = (1 + r)I(3t_{constant} + t_{experiment}), \quad (4)$$

C_{bat} stands for battery capacity, r stands for margin rate, I for current through electrodes, $t_{constant}$ for the time constant of the superconductor magnet circuit, and $t_{experiment}$ for the actual duration of ship movement. While a larger battery capacity is desirable, it is important to consider the impact of the battery's weight on the overall drag experienced by the ship. Therefore, the optimal battery configuration is one with a minimum capacity that is still greater than the required value.

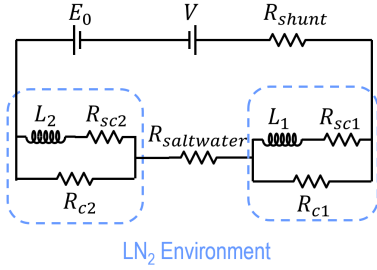


Fig. 2. Lumped circuit of MHD ship. Current passes through R_{shunt} , coil 1, $R_{saltwater}$, coil 2. Coil 1 and coil 2 are both in LN_2 environment to maintain superconductivity.

III. EXPERIMENT SETUP

A. Electromagnetic&circuit: series connection of battery and superconductor magnet

Figure 3 shows an overall configuration of the MHD ship system with NI HTS magnet. Current starts to flow from the anode of the LiPo battery. It passes through the shunt resistor, which is $0.77 \text{ m}\Omega$, and flows through the first HTS coil. Then, it arrives at the anode of the electrode pair. Current passes through the saltwater, in which electrolysis happens, and flows

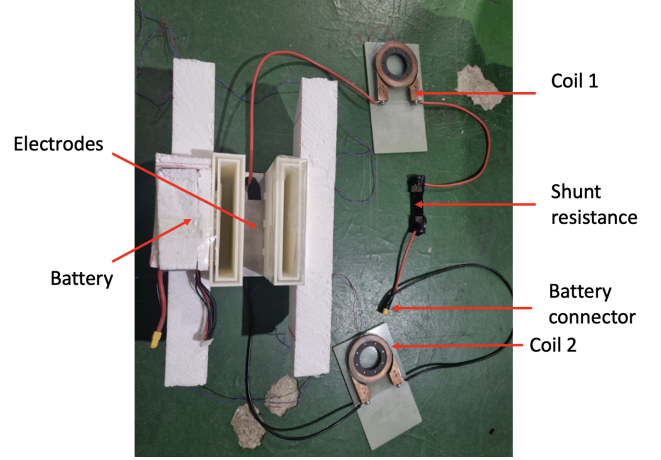


Fig. 3. Overall view of MHD ship system. Once the battery is connected, the current flows through the battery, shunt resistor, coil 1, electrodes, and coil 2.

through the cathode of the electrode pair and the second HTS coil. Lastly, the current arrives at the cathode of the battery.

Initially, attempts were made to charge the magnets and flow current through electrodes using a power supply. Unfortunately, the weight and friction of the current-carrying cable outweighed the ship's thrust, which is on the order of 100 mN , leading to imprecise measurements of the ship's motion. To address this issue, the superconducting magnets are connected in series with the electrodes linked to the battery, and the whole circuit is mounted on the preliminary magnetohydrodynamic ship to move in unison. If solely the superconducting magnets were linked to the battery, there would be concerns regarding operational stability due to excessive current. Nevertheless, computations based on the resistivity of saltwater reveal that the current flowing through the superconducting magnets is lower than the critical current value.

Since the thrust of the ship is 185 mN , which is on the level at which errors due to friction cannot be ignored, to minimize the interference due to external forces such as friction that originates from power cables, the circuit is designed to be closed loop installed to the ship.

B. Thermal & fluid-dynamics: hull with thermal insulation

The construction of the containers for the experiment involves the utilization of a Sindoh 3DWOX 1 3D printer, employing PLA filaments. To ensure buoyancy, Styrofoam is employed for floats due to its lightweight nature compared to plastic materials. While the mechanical stability of the design is reinforced through the use of PLA filaments, challenges associated with the low-temperature environment of 77 K necessitate additional considerations. Firstly, the battery is prone to performance degradation at low temperatures, as documented in previous research [36]. To mitigate this issue, a Styrofoam plate, with a thickness of 20 mm , is employed to insulate the battery from the container, providing a thermal barrier against extreme cold. Secondly, the inherent brittleness of plastic materials at 77 K , given its significantly lower operating temperature compared to its freezing point [37],

poses a potential challenge. To address this concern, a practical solution involves using a zipper bag to prevent direct contact of the containers with liquid nitrogen (LN_2), thus minimizing the risk of brittleness and ensuring the structural integrity of the components. In the context of a saltwater environment, attaining a 30 % saltwater concentration necessitates the dissolution of salt into water. For our study, salt was meticulously dissolved to near its maximum solubility threshold to enhance the performance of the ship. Once the magnets transition into the superconducting state, the battery is connected to the circuit. Approximately three time constants later, the experimental setup demonstrates observable motion, propelled by the Lorentz force generated in the superconducting state. This temporal sequence highlights the intricate interplay of material choices, thermal considerations, and experimental procedures crucial for the successful execution of the MHD propulsion experiment in a cryogenic environment.

IV. RESULTS

A. Electromagnetic results: operating current, center magnetic field, and voltage of each coil

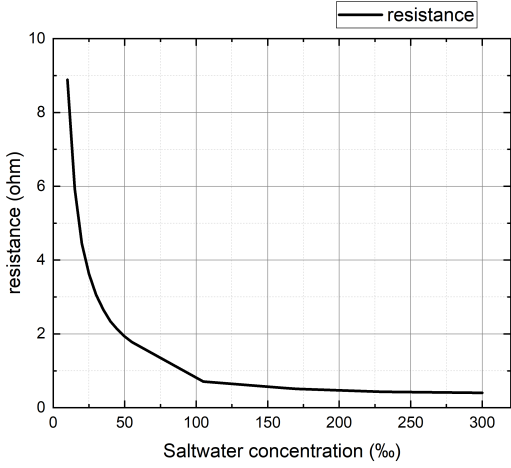


Fig. 4. Resistance of saltwater according to the inter-electrode gap and saltwater concentration. Under 300%, the resistance is expected to be 0.40 m Ω [38].

Figure 4 shows a resistance graph which is calculated regarding the gap between electrodes and saltwater concentration, using the data of saltwater conductivity expressed in [38]. Besides saltwater resistance, overpotential also should be considered. Assuming the steady superconducting state, since R_{sc1} , R_{sc2} , L_1 , and L_2 in fig. 2 can be neglected, LN_2 environment can be considered as a short circuit.

$$V = E_0 + I(R_{shunt} + R_{saltwater}) + v_{thruster} BH, \quad (5)$$

where V stands for the battery voltage, E_0 for the voltage used for initiating the electrolysis of water, which is 1.23 V. R_{shunt} and $R_{saltwater}$ stand for shunt resistance, and the resistance of saltwater, which is 0.4 Ω , B for the magnetic field, H for an inter-electrode gap, $v_{thruster}$ for the water velocity

inside the thruster, and I for our current that flows through saltwater. $v_{thruster} BH$ expresses the reverse voltage due to the movement of ions. The reverse voltage and the resistance of the shunt can be neglected since both are below 1% of the total voltage and resistance. According to the eq. (5), the total operating current from the system of the whole system turns out to be 54.4 A. However, the actual current turns out to be 70.0 A, which is 28.7% larger than we expected. The result may be affected by the rising temperature of water due to the high current that flows through electrodes. For additional circuit parameters, through prior research, the inductances of each coil turns out to be 2.19 mH, 2.12 mH, and resistances, 156 m Ω , 98 m Ω , respectively.

Figure 5 shows the voltage and center field graph of each coil. The result of the experiment well aligns with that of the simulation based on obtained values of inductance and resistance. The operating current shows a step response of 70.0 A as soon as the circuit close. The center magnetic field increases gradually until saturation towards 0.18, 0.19 T. Coil voltage spikes to 10 mV and decreases rapidly as the current in the radial direction saturates.

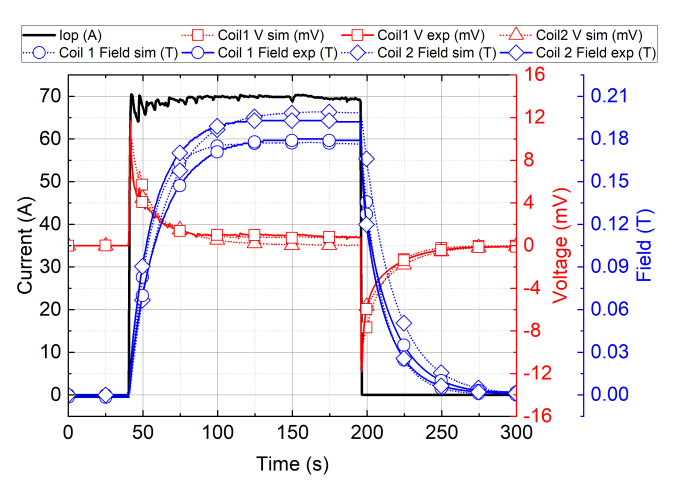


Fig. 5. Measured and simulated results of MHD ship. Under an operating current of 70.0 A, center magnetic fields are 0.18 T and 0.19 T each. Data regarding actual propulsion is collected from 150 s to 170 s since the ship moved at that interval.

B. Thermal results: evaporation of LN_2 throughout the experiment

The liquid nitrogen (LN_2) evaporated as expected during the experiment, keeping the level consistent. When the zipper bag was torn or the 3D printer filament broke, LN_2 disappeared more quickly. However, even with these incidents, we didn't have to add more liquid nitrogen while the ship was moving. This shows that the experiment stayed on track and the MHD propulsion system worked well, handling unexpected situations without needing extra LN_2 .

C. Fluid-dynamics results: forward velocity and rotation angle

The force balance equation can be derived based on the Navier-Stokes theorem which is expressed in eq. (6) [16].

$$v\nabla v = -\nabla P + \nu\nabla^2 v + J \times B, \quad (6)$$

where v stands for the velocity field, P for pressure, J for current density, ν for kinematic viscosity, and B for magnetic flux density.

Equation (7) shows the derived equation. The left-hand side of the equation shows the total Lorentz force of the ship, and the right-hand side expresses the total loss of the ship.

$$\begin{aligned} BIH = & \frac{1}{2}\rho S_{wet} \frac{0.664}{\sqrt{Re}} v_{ship}^2 + \frac{1}{2}\rho C_{form} S_{forward} v_{ship}^2 + \\ & \frac{1}{2}f \frac{L}{D} \rho S_{thruster} v_{thruster}^2 + \\ & \frac{1}{2}\rho S_{thruster} (C_{pipe\ in} + C_{pipe\ out})(v_{thruster}^2 - v_{ship}^2), \end{aligned} \quad (7)$$

where B stands for magnetic field, I for electric current, H gap between electrodes, $\frac{0.664}{\sqrt{Re}}$ stands for the skin friction coefficient calculated according to Blasius solution of skin friction coefficient [39], S_{wet} for the total wet surface, ρ for the density of saltwater, v_{ship} for the ship's velocity, $S_{forward}$ for the frontal surface of the ship, C_{form} for the coefficient of form drag force. Re stands for the Reynolds number, which is derived from the characteristic length of our ship. The characteristic length of our ship is calculated by summing up the inner flow of our ducts and the outer flow of our outer ship structure. It turns out to be 12 cm. Dynamic viscosity data of saltwater is from [40]. S_{wet} is calculated as 2326 cm², considering the immersion depth of our float as 2.2 cm. C_{form} , which is the coefficient of drag force, is 1.05 to the data of [41]. $S_{forward}$ is calculated as 109.12 cm². f stands for Darcy friction factor, L for the length, D for the inner diameter of the thruster, $S_{thruster}$ for the cross-sectional surface of the thruster. $C_{pipe\ in}$ and $C_{pipe\ out}$ stand for the coefficient of loss regarding the inlet and outlet of the pipe, which is calculated as 1.0 each according to [41].

The first loss is the skin friction force of our whole ship. It is proportional to the skin friction coefficient, the total wet surface, the density of saltwater, and the square of the ship's velocity. The second loss is the form drag force of our ship. It is proportional to the cross-sectional surface of the thruster, the density of saltwater, and the square of the ship's velocity. The third loss is the loss that is caused inside the thruster. It is proportional to the Darcy friction factor, the length of the thruster, the cross-sectional surface of the thruster, the density of saltwater, and the square of the water's velocity inside it. It is inverse-proportional to the inner diameter of the thruster. The Darcy friction factor is calculated as $64/Re$, using the Hagen-Poiseuille law. The length of the thruster is calculated as 150 mm, and the inner diameter as 41 mm. The cross-sectional surface of the thruster is calculated as 17.28 cm². The fourth loss is the loss that is caused at the inlet and outlet

of the thruster. It is proportional to the density of saltwater. It is also proportional to the loss coefficient and the square of the relative velocity of saltwater in the thruster, from the perspective of the ship.

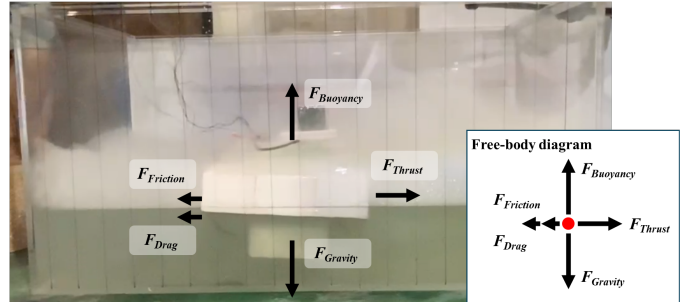


Fig. 6. Free Body Diagram of an MHD Ship. The buoyant force arising from flotation counteracts the gravitational force to prevent submersion, while the Lorentz's force propels the ship forward. This propulsive force is counterbalanced by resistive forces, including friction and drag.

Figure 6 presents the free body diagram of the ship. The buoyancy, provided by the design of the float, is engineered to offset the ship's weight as detailed in eq. 3. The expected velocity of the ship is derived from the equilibrium between the Lorentz force, shown on the left side of the figure, and the sum of resistive forces on the right, as established in eq. 7.

Equation 8 shows the relationship of the force that water and ship pushed in the opposite direction.

$$\begin{aligned} \dot{m}(v_{thruster} - v_{ship}) = & \frac{1}{2}\rho S_{wet} \frac{0.664}{\sqrt{Re}} v_{ship}^2 + \\ & \frac{1}{2}\rho C_{form} S_{forward} v_{ship}^2, \end{aligned} \quad (8)$$

The force should be equal to the sum of the skin drag force and the form drag force of the ship. \dot{m} is the mass flow rate of saltwater, which can be expressed as $S_{thruster}v_{thruster}$. The formula also means that Lorentz force, except the loss due to internal loss in the pipe, is used to move the actual ship, overcoming the skin and form drag force. The ratio of $v_{thruster}$ and v_{ship} , α , is calculated as follows.

$$\begin{aligned} \alpha = & \frac{v_{thruster}}{v_{ship}} \\ = & \frac{1}{2} + \sqrt{\frac{1}{4} + \frac{1}{2}S_{wet} \frac{0.664}{\sqrt{Re}} + \frac{1}{2}C_{form} S_{forward} S_{thruster}}, \end{aligned} \quad (9)$$

Since we have two formulas regarding two unknown values, v_{ship} , and $v_{thruster}$, the system is closed, and every theoretical parameter can be calculated. The terminal velocity is expected to be 9.6 cm/s.

Figure 7 depicts the movement patterns of our experimental ship over time. Notably, After 16 seconds, it can be seen that the rotation angle increases significantly. Theoretically, the terminal velocity is expected to be 9.6 cm/s. However, the velocity saturates to about 4.0 cm/s until 12 s and starts to rotate, significantly decreasing the forward velocity. The ship's motion can be categorized into three distinct phases

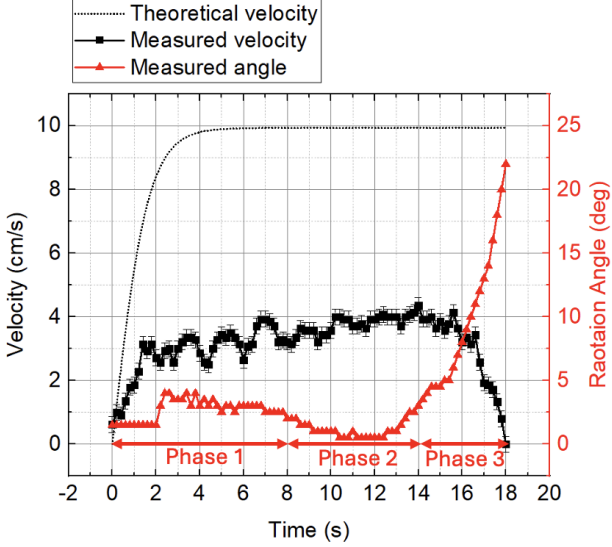


Fig. 7. Measured velocity, the rotation angle, and theoretical velocity of the tested MHD ship. “Theoretical velocity” and “Measured velocity” both mean scalar values of forward velocity.

based on these observations. In the first phase, the ship moves forward at an increasing speed as it vibrates. It is due to the vertical wave that is generated by the movement of the ship. In the second phase, the velocity of the ship is saturated to about 4.0 cm/s. In the third phase, the velocity of the ship declines significantly since the rotational movement became dominant. A rotational movement can be seen in fig. 8. The forward velocity is calculated by analyzing the video of ship movement sampled three times per second. The line is drawn at 5 cm intervals in the tank, which is used in the experiment to measure distance.

The position of the ship at each stage and the angle at which the ship turned can be confirmed through fig. 8. Rotation of the test ship appears to be caused by two factors: imbalance due to asymmetry and repulsion due to the tank walls. First of all, homemade floats made of Styrofoam are not exactly symmetrical in size and attachment location. In addition, there is an imbalance in weight due to the inability to accurately control the remaining amount of nitrogen. Second, it is assumed that the repulsive force caused by waves reflected on the tank wall was one of the factors preventing the ship from moving in a straight line.

D. Circuit results: superconductor magnet-battery connection and time constant

As illustrated in Figure 5, the experimental results reveal a noteworthy trend. Within three time constants, equivalent to 60 seconds, the target magnetic field is attained, reaching a substantial 90-95% of the desired value. Following this phase, the ship is released from fixation and initiates motion. Notably, the voltage of the battery remains constant throughout the entire experiment. Furthermore, the superconductor magnets, integrated in series with the battery, contribute to the overall success of the experiment. This integration ensures the safety

of the operation, as evidenced by the absence of mechanical, electromagnetic, or thermal failures and quench events.

V. SCALE-UP DESIGN

In this section, the parameters for a scaled-up version of the MHD thruster based on experimental results are presented. The geometric parameters are the same as those of Yamato-1 but the low-temperature superconductor (LTS) magnets with insulation are replaced with NI HTS REBCO magnets. Electromagnetic and thermal designs that can maximize the performance of NI HTS magnets using currently commercially available REBCO tape are presented. This section also includes the mechanical design due to the Lorentz force under high magnetic field conditions. However, a discussion of fluid-dynamics is excluded from this section as it can vary greatly depending on the condition of the state of the fluid according to the shape and speed of the ship. Table III shows the key parameters of the overall system of the designed scale-up MHD thruster, compared with the corresponding values of Yamato-1. The simulation results are presented using COMSOL Multiphysics®.

TABLE III
KEY PARAMETERS OF THE NI HTS SCALE-UP DESIGN VS YAMATO-1

Parameters	Units	Value	
Magnet Parameters		NI HTS	Yamato-1
Superconductor		REBCO	NbTi
Gap between straight sections	[m]	0.36	
Length of straight section	[m]	3.0	
Operating temperature	[K]	20	4
Critical current at operating current	[A]	943	-
Operating current	[A]	350	2,080
Engineering current density	[A/mm ²]	292	105
Conductor width; thickness	[mm]	12; 0.1	11; 1.8
Total conductor length	[km]	1,358	82
Total conductor weight	[ton]	10.4	12.8
Inductance	[H]	41.2	-
Charging time constant	[hour]	2.74	-
Thruster parameters			
Electrode width;length	[m]	0.13 ; 3	
Electrode gap*	[cm]	175	
Voltage*	[V]	150	
Resistance*	[mΩ]	74	
Volumetric average field	[T]	5.6	1.9
Current*	[A]	2,000	
Power input for propulsion	[kW]	3,600	
Power input for cooling	[kW]	7.5	37.5
Number of thrusters		12	
Lorentz force	[kN]	23.3	8.4
Maximum Von Mises stress	[MPa]	500	65

* Between electrodes, per thruster

A. Electromagnetic design: 292 A/mm² of current density and 5.5 T of magnetic field with 63% current margin with REBCO NI HTS magnets at 20 K

The first consideration in the design of a superconducting magnet is to ensure the operating conditions, especially the

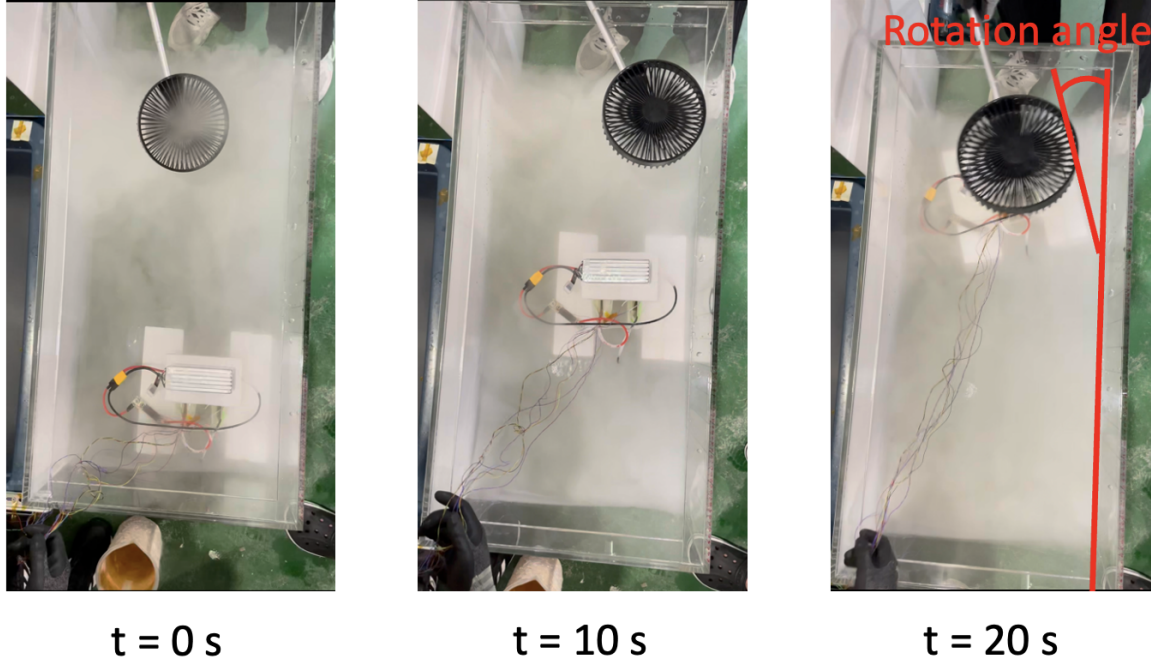


Fig. 8. Experimental images at $t = 0 \text{ s}$, $t = 10 \text{ s}$, and $t = 20 \text{ s}$. The tested MHD ship starts with one side against the wall of the water tank and moves mostly only forward until it starts a large rotational motion after $t=10 \text{ s}$.

operating current, do not exceed critical conditions, otherwise a "quench" phenomenon, where the superconducting state is lost, can occur and damage the magnet. At an operating temperature of 20 K, a critical current of 943 A is calculated under an operating current of 350 A when Superpower Inc.'s 12 mm wide, 100 μm thick REBCO HTS tape is applied to the magnet geometry of Yamato-1. This results in a current margin of 62.9%, at which point the engineering current density of the HTS magnet is calculated to be 292 A/mm². The total length of REBCO tape used in the magnet is 1,358 km. Data from the Robinson Research Institute are used in the calculation of the critical current [42]. The designed magnet has the same shape and size as the saddle unit magnet used in Yamato-1, and there are 12 thrusters each made up of unit magnet pairs. The spatial average magnetic field in the duct area is calculated to be 5.6 T at the operating current of 350 A. Figure 9 shows the magnetic field distribution in the duct area. At the electrical conductivity of seawater, 6 S/m, the resistance between the designed electrodes is 74 m Ω , and when a voltage of 150 V is applied to each thruster, a current of 2,000 A is conducted between each electrode pair. The Lorentz force induced by the magnetic and electric fields is 23.3 kN.

B. Thermal design: 7.5 kW of cooling power required 'without coolant' to cool down conductive heat intrusion through the current lead

The operating temperature of the designed REBCO NI HTS magnet is set at 20 K, and instead of using a coolant such as liquid helium, a cryocooler is used for cooling. With a vacuum below 10^{-4} torr and the heat transfer by convection and radi-

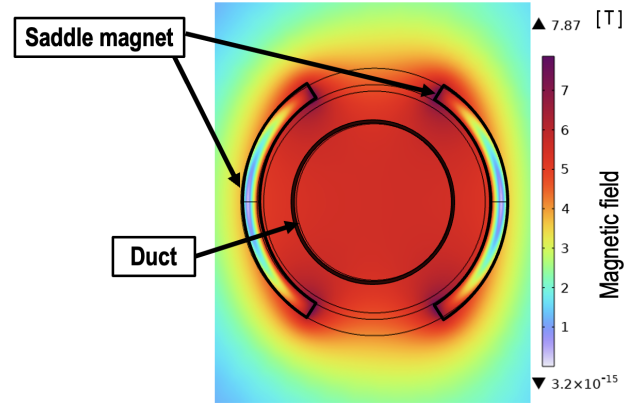


Fig. 9. Magnetic field distribution around a unit thruster. The volumetric average field throughout the duct is 5.6 T. The MHD ship is composed of 12 thrusters.

ation blocked by installing a radiation shield and appropriate multi-layer insulation, heat intrusion by conduction through the current leads is the dominant heat source.

Assuming that copper is used as the lead for the current supply from T_0 to T_1 and REBCO tape from T_1 to T_2 , the heat input by conduction is calculated as follows [43]:

$$Q_{Cu} = I_{op} \sqrt{2k_{Cu} \rho_{Cu} (T_0 - T_1)}, \quad (10)$$

$$Q_{HTS} = \bar{k}_{HTS} S_{HTS} \frac{(T_1 - T_2)}{l_{HTS}}, \quad (11)$$

where Q_{Cu} and Q_{HTS} stand for heat intrusion from the copper and HTS respectively, I_{op} for operating current, \bar{k} and $\bar{\rho}$ for temperature averaged thermal conductivity and electrical resistivity, and S_{HTS} and l_{HTS} for the cross-sectional area and the length of the HTS current lead, respectively. In the case of our design, T_0 , T_1 , and T_2 are 300 K, 77 K, and 20 K, which yields the total heat intrusion from the current lead is about 15 W. The ratio of the required energy for cooling a 15 W heat with a cryocooler from 300 K to 20 K is about 500 [43], so it is calculated that 7.5 kW is required for cooling power.

C. Mechanical design: 500 MPa of peak stress without support structure

Under high magnetic fields, the stresses and resulting strains applied to the tape by the Lorentz force act as one of the main parameters governing the superconducting properties. In general, it is known that REBCO tapes significantly lose their conventional superconducting properties when the stress is around 600 MPa. Under the operating conditions of this design, it is calculated that a von Mises stress of 500 MPa is applied to the straight section of fig. 10. A roller boundary condition is imposed on the top surface of the straight section and the center surface of the curved section, and no additional reinforcing structures are assumed. Techniques such as adding support structures and overbanding are commonly used to reduce the stresses on HTS magnets. However, there is still much to be learned about the stresses of the saddle type, especially in curved areas. [44], [45]

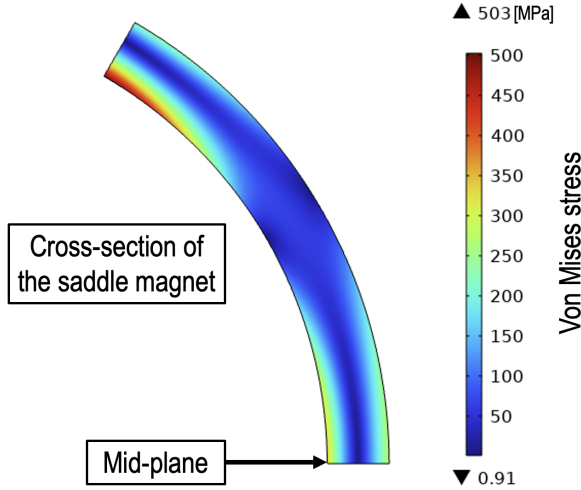


Fig. 10. 2D stress calculation results when the top half of the saddle magnet design is set as the calculation area, and a roller boundary condition is imposed at the mid-plane and last turn. The maximum calculated von Mises stress in the straight section is calculated to be 500 MPa.

D. Operational design: 2.7 h of time constant by lumped circuit model

The characteristic resistance of each thruster designed is calculated as $348 \mu\Omega$ with a contact resistivity of $20 \mu\Omega \text{ cm}^2$. Given the inductance 41.2 H of the thruster, the charging time

constant is calculated as 2.74 hour. Recently, the metal insulation (MI) technique, a variation of the so-called no-insulation (NI) class techniques for HTS magnets, was proposed to compensate for the long charging time of the magnet due to the high leakage current of NI HTS magnets [22]. NI-class HTS magnets are modeled as an equivalent circuit called a lumped circuit in Fig.2, and the higher the characteristic resistance of the circuit, the shorter the charging time. The contact resistivity, which determines the characteristic resistance, is known to be about 100 times greater for MI than for NI, which means that charging time can be shortened by more than 100 times under the same configuration. Typically, the contact resistivity of MI magnet is reported to be more than about $1,000 \mu\Omega \text{ cm}^2$ [22]. Based on this, the characteristic resistivity and time constant are calculated as 0.174Ω and 19.7 seconds, respectively.

VI. DISCUSSION

Using formulas in section IV-C, the expected terminal velocity is 9.6 cm/s. The expected velocity of the ship according to time is shown in fig. 7. As stated in section IV-C, the measured terminal velocity is 4.0 cm/s, which is 42% of the expected value. In our error analysis, the assumptions underlying the fluid dynamics calculations are evaluated, with a particular focus on the previously overlooked factor: the absolute velocity of water external to a duct in the context of the ship's design. This oversight has the potential to result in an underestimated drag force when compared to actual conditions, which, in turn, could lead to an overestimation of the ship's velocity. This is particularly pertinent considering the interaction between the water flow and the thruster, as the water flow being drawn into the thruster influences the surrounding flow dynamics. While reference [46] offers a fluid dynamics analysis of velocity distribution around the inlet of a pipe, its relevance is constrained by the differences in design.

Additionally, two other reasons contribute to the complexity of the analysis : waves from reflections due to the small size of the water tank, and friction from signal lines. These are also supposed to be the main causes.

Table III presents key performance parameters for both the MHD ship with NI HTS and Yamato-1. In general, there are three main considerations when building an electrical device: cost, reliability, and performance. The costs for the proposed scale-up MHD can be divided into two main categories: manufacturing and operation. At this point, due to the high cost of HTS tape, superconducting magnets are likely to account for the majority of the cost of the MHD system. The operating costs of an MHD system include power supplement for propulsion and cooling. The power for propulsion is 300 kW per thruster and 3,600 kW in total. 7.5 kW of cooling power is required for the cooling of NI HTS MHD system. In the case of Yamato-1, the expected heat invasion was 7 W, where in fact it was 15 W. Yamato-1 is pre-cooled with helium gas to 20 K, followed by "wet cooling" with liquid helium to 4 K. In comparison, NI HTS magnets of the scale-up design use "dry cooling" which uses heat conduction, to 20 K. Typically, a two-stage Gifford-McMahon cryocooler is used, and given

the COPs from 300 K to 20 K, this requires about 500 times the power of the heat generated. This increases to about 2,500 times for 4 K, so it would take about 37.5 kW to cool a 15 W Yamato-1 [43]. The total price of NbTi and REBCO conductors are calculated to be about 0.4 M\$ and 20 M\$, respectively. Just as the demand for MRI has driven down the price of LTS wire [47], the rapidly increasing demand for HTS tape in compact fusion magnets has recently been observed to drive down the price [48], [49]. The estimated power cost for propulsion for Yamato-1 and scale-up design are both 605 \$/h, and the cooling costs are 6.3 \$/h, and 1.3 \$/h, respectively.

The reliability of superconducting magnets can be broadly divided into two characteristics: stability, which prevents the phenomenon of quench, in which the magnet loses its superconductivity; and protection, which prevents the magnet from burning out when quenching occurs. Stability is determined by the enthalpy difference between the operating temperature and the critical temperature, and in general, the stability margin of HTS is about 500 times higher than that of LTS [43]. As such, the LTS magnets can undergo quench and generate additional heat for even small disturbances such as wire motion, so a “wet cooling” method is commonly used to effectively cool them. In the case of critical current, a margin of about 62.9% is calculated for NI HTS magnet by considering the critical current 943 A, which is calculated under the operating current of 350 A. The critical current data for Yamato-1 is not available to the best of our knowledge. Even if a quench occurs in NI HTS magnet for some reason, the self-protection capability of the NI magnet prevents burnout of the magnet [19]. For the performance of the designed NI HTS thruster, the propulsion system using NI HTS operates at a higher operating temperature of 20 K compared to 4 K for LTS. However, assuming the same configuration, voltage, and current between the electrodes, the current density, average magnetic field energized in the magnets, and hence the Lorentz force increases by about 2.8 times. This is the performance limit due to the stresses on the REBCO tape and higher performance can be expected if additional reinforcement structures are built or tape strength is improved.

MHD propulsion system exhibits lower efficiency compared to conventional motors and raises concerns regarding environmental impact, particularly the diffusion of chloride into seawater. It also faces structural challenges such as electrode corrosion due to extensive electrolysis. However, these challenges can be effectively addressed by implementing various solutions. Regarding efficiency, as the MHD ship scales up, its efficiency can increase rapidly in proportion to magnetic field density. To mitigate the environmental issue of chloride diffusion into seawater, a containment system can be incorporated into the design to intercept and neutralize chloride before it poses a threat to marine animals or passengers. To tackle the problem of electrode corrosion, employing materials such as stainless steel for the electrodes diminishes concerns related to corrosion [16]. These strategies hold promise in enhancing the performance and sustainability of MHD propulsion systems, paving the way for their broader adoption in marine applications. Although efficiency remains a critical factor for market viability, it's undeniable that the MHD ship possesses

strengths tailored to address inherent problems in existing motors, positioning it as a promising solution for certain niche applications. Further development and refinement are essential to fully unlock the potential of the MHD propulsion system in the maritime industry. Lastly, it's worth noting that this study represents unprecedented experimental research into the application of No-Insulation technology combined with MHD propulsion systems. It is expected to serve as foundational research for further applications of MHD technology to propulsion systems, contributing to advancements in marine engineering and transportation technology.

VII. CONCLUSION

In conclusion, the feasibility study of MHD propulsion utilizing a REBCO NI HTS magnet has been successfully conducted through the design and testing of a miniature ship within a liquid nitrogen environment (77 K). The voltage and magnetic fields measured in charge and discharge tests of NI HTS magnets for miniature ships are in reasonable agreement with theoretical calculations. The addition of an insulating layer around the container ensured the maintenance of a sufficient level of liquid nitrogen for cooling during the experiment. The ship, under specified parameters and operating conditions, demonstrated a gradually saturating velocity, with the actual experiment showing a saturated velocity within the range of 4.0 cm/s to 5.0 cm/s. Despite a 58% error in fluid-dynamics calculations between experimental and simulated ship speeds, it is anticipated that various factors contributed to this discrepancy. The NI HTS magnet, integrated in series with the battery, proved to be safe throughout the experiment, and an optimum battery capacity of 2200 mAh was determined based on anticipated electric power consumption over 80 seconds.

The scale-up design of the NI-HTS applied MHD ship, modeled after the Yamato-1, involves 12 pairs of saddle magnets generating an average magnetic field of 5.6 T and a Lorentz force of 23.3 kN at a current density of 292 A/mm² at 20 K. These performance parameters surpass those of Yamato-1 by 177.4%, operating at 4 K. The main heat source, conduction heat from current leads, is effectively managed through a “dry cooling” method consuming 7.5 kW of power. Stress analysis, without a support structure, revealed a limiting parameter of 500 MPa for achieving higher propulsion performance. Furthermore, employing the NI method yielded a charge and discharge time constant of approximately 2.7 hours, which can be significantly reduced to 19.7 seconds with the application of the MI method. This research provides valuable insights into the potential of NI-HTS applied MHD propulsion for future developments in advanced space propulsion systems.

REFERENCES

- [1] P. A. Davidson, “The role of pressure forces in mhd propulsion of submersibles,” *Nav. Eng. J.*, vol. 104, no. 5, pp. 39–42, 1992.
- [2] A. A. Bednarczyk, “Nuclear electric magnetohydrodynamic propulsion for submarine,” Massachusetts Inst of Tech Cambridge, Tech. Rep., 1989.
- [3] D. W. Swallom, I. Sadovnik, J. S. Gibbs, H. Gurol, L. V. Nguyen, and H. H. Van Den Bergh, “Magnetohydrodynamic submarine propulsion systems,” *Nav. Eng. J.*, vol. 103, no. 3, pp. 141–157, 1991.

- [4] O. Al-Hababbeh, M. Al-Saqqa, M. Safi, and T. Khater, "Review of magnetohydrodynamic pump applications," *Alexandria Engineering Journal*, vol. 55, 03 2016.
- [5] B. Ji, X. Luo, X. Peng, Y. Wu, and H. Xu, "Numerical analysis of cavitation evolution and excited pressure fluctuation around a propeller in non-uniform wake," *International Journal of Multiphase Flow*, vol. 43, pp. 13–21, 2012.
- [6] L. Yan, C. Sha, Y. Peng, K. Zhou, A. Yang, and Q. Qing, "Results from a 14t superconducting mhd propulsion experiments," in *33rd plasmadynamics and lasers conference*, 2002, p. 2172.
- [7] Y. Peng, C. Sha, K. Zhou, A. Yang, and A. Peng, "Superconducting mhd helical channel experimental ship "hems-1"," in *The Fifteenth International Offshore and Polar Engineering Conference*. OnePetro, 2005.
- [8] L. Yan, Z. Wang, C. Xue, Z. Gao, and B. Zhao, "Development of the superconducting magnet system for hems-1 mhd model ship," *IEEE Trans. Appl. Supercond.*, vol. 10, no. 1, pp. 955–958, 2000.
- [9] L. Yan, C. Sha, K. Zhou, Y. Peng, A. Yang, and J. Qin, "Progress of the mhd ship propulsion project in china," *IEEE Trans. Appl. Supercond.*, vol. 10, no. 1, pp. 951–954, 2000.
- [10] J. Chen, D. Wang, W. Huang, S. Jin, and H. Zhu, "Feasibility analysis of helical superconducting mhd propulsor for naval vessels," *IEEE Trans. Appl. Supercond.*, vol. 29, no. 2, p. 3600407, 2018.
- [11] H. Jiang, Y. Peng, L. Zhao, C. Sha, Z. Lin, and R. Li, "Three-dimensional numerical simulation on helical channel mhd thruster," in *2008 International Conference on Electrical Machines and Systems*. IEEE, 2008, pp. 4150–4154.
- [12] L. Zhao, Y. Peng, J. Li, L. Fang, C. Sha, Y. Xu, R. Li, and B. Liu, "Experimental study on superconducting helical channel mhd thruster," in *42nd AIAA Plasmadynamics and Lasers Conference in conjunction with the 18th International Conference on MHD Energy Conversion (ICMHD)*, 2011, p. 3590.
- [13] Y. Sasakawa, S. Takezawa, Y. Sugawara, and Y. Kyotani, "The superconducting mhd-propelled ship yamato-1," in *NASA Johnson Space Center, Proceedings of the 4th International Conference and Exhibition: World Congress on Superconductivity, Volume 1*, 1995.
- [14] Y. Sasakawa, S. Takezawa, and K. Sugawara, "Outline of r&d of the superconducting mhd ship yamato-1," in *The Third International Offshore and Polar Engineering Conference*. OnePetro, 1993.
- [15] P. Hales, P. Hirst, S. Milward, S. Harrison, and H. Jones, "A solid-nitrogen cooled high-temperature superconducting magnet for use in magnetohydrodynamic marine propulsion," *IEEE Trans. Appl. Supercond.*, vol. 16, no. 2, pp. 1419–1422, 2006.
- [16] D. Cébron, S. Viroulet, J. Vidal, J.-P. Masson, and P. Viroulet, "Experimental and theoretical study of magnetohydrodynamic ship models," *PloS One*, vol. 12, no. 6, p. e0178599, 2017.
- [17] J. G. Bednorz and K. A. Muller, "Possible high Tc superconductivity in the Ba-La-Cu-O system," *Z. Phys. B*, vol. 64, pp. 189–193, 1986.
- [18] M. K. Wu, J. R. Ashburn, C. J. Torng, P. H. Hor, R. L. Meng, L. Gao, Z. J. Huang, Y. Q. Wang, and C. W. Chu, "Superconductivity at 93 K in a new mixed-phase $\text{y}-\text{ba}-\text{cu}-\text{o}$ compound system at ambient pressure," *Phys. Rev. Lett.*, vol. 58, pp. 908–910, Mar 1987. [Online]. Available: <https://link.aps.org/doi/10.1103/PhysRevLett.58.908>
- [19] S. Hahn, D. K. Park, J. Bascuñán, and Y. Iwasa, "HTS pancake coils without turn-to-turn insulation," *IEEE Trans. Appl. Supercond.*, vol. 21, no. 3, pp. 1592–1595, 2011.
- [20] X. Wang, S. Hahn, Y. Kim, J. Bascunan, J. Voccio, H. Lee, and Y. Iwasa, "Turn-to-turn contact characteristics for an equivalent circuit model of no-insulation ReBCO pancake coil," *Supercond. Sci. Technol.*, vol. 26, no. 3, p. 035012, 2013.
- [21] D. Uglietti, R. Wesche, and P. Bruzzone, "Construction and test of a non-insulated insert coil using coated conductor tape," *J. Phys.: Conf. Ser.*, vol. 507, no. 3, p. 032052, 2014.
- [22] T. Lécrevisse and Y. Iwasa, "A (RE) BCO pancake winding with metal-as-insulation," *IEEE Trans. Appl. Supercond.*, vol. 26, no. 3, p. 4700405, 2016.
- [23] S. Hahn, D. K. Park, J. Voccio, J. Bascunan, and Y. Iwasa, "No-Insulation (NI) HTS inserts for >1 GHz LTS/HTS NMR magnets," *IEEE Trans. Appl. Supercond.*, vol. 22, no. 3, p. 4302405, 2012.
- [24] S. Hahn, Y. Kim, D. Keun Park, K. Kim, J. P. Voccio, J. Bascuñán, and Y. Iwasa, "No-insulation multi-width winding technique for high temperature superconducting magnet," *Applied physics letters*, vol. 103, no. 17, p. 173511, 2013.
- [25] J. B. Song and S. Y. Hahn, "'Leak current' correction for critical current measurement of no-insulation HTS coil," *Prog. Supercond. Cryogenics*, vol. 19, no. 2, pp. 48–52, 2017.
- [26] T. Lécrevisse, A. Badel, T. Benkel, X. Chaud, P. Fazilleau, and P. Tixador, "Metal-as-insulation variant of no-insulation hts winding technique: pancake tests under high background magnetic field and high current at 4.2 k," *Supercond. Sci. Technol.*, vol. 31, no. 5, p. 055008, 2018.
- [27] T. Painter, K. Kim, K. Kim, K. R. Bhattachari, K. Radcliffe, H. Xinbo, S. Bole, B. Jarvis, I. Dixon, S. Hahn, and D. Larbalestier, "Design, construction and operation of a 13 T 52 mm no-insulation REBCO insert for a 20 T all-superconducting user magnet," *Rev. Sci. Instrum.*, 2017.
- [28] J. Bascuñán, S. Hahn, T. Lécrevisse, J. Song, D. Miyagi, and Y. Iwasa, "An 800-MHz all-REBCO insert for the 1.3-GHz LTS/HTS NMR magnet program—a progress report," *IEEE Trans. Appl. Supercond.*, vol. 26, no. 4, p. 4300205, 2016.
- [29] T. Painter, K. Kim, K. Kim, K. Bhattachari, K. Radcliffe, H. Xinbo, S. Bole, B. Jarvis, I. Dixon, S. Hahn *et al.*, "Design construction and operation of a 13 t 52 mm no-insulation rebc0 insert for a 20 t all-superconducting user magnet," in *25th Int. Conf. Magnet Technol.*, 2017.
- [30] J. Liu, Y. Dai, and L. Li, "Progress in the development of a 25 T all superconducting NMR magnet," *Cryogenics*, vol. 79, pp. 79–84, 2016.
- [31] S. Hahn, J. Song, Y. Kim, T. Lécrevisse, Y. Chu, J. Voccio, J. Bascuñán, and Y. Iwasa, "Construction and test of 7-T/68-mm cold-bore multiwidth no-insulation GdBCO magnet," *IEEE Trans. Appl. Supercond.*, vol. 25, no. 3, p. 4600405, 2015.
- [32] S. Yoon, J. Kim, K. Cheon, H. Lee, S. Hahn, and S.-H. Moon, "26 t 35 mm all-gdba2cu3o7-x multi-width no-insulation superconducting magnet," *Supercond. Sci. Technol.*, vol. 29, no. 4, p. 04LT04, 2016.
- [33] J.-B. Song, X. Chaud, B. Borgnic, F. Debray, P. Fazilleau, and T. Lécrevisse, "Construction and test of a 7 t metal-as-insulation hts insert under a 20 t high background magnetic field at 4.2 k," *IEEE Trans. Appl. Supercond.*, vol. 29, no. 5, p. 4601705, 2019.
- [34] S. Hahn, K. Kim, K. Kim, X. Hu, T. Painter, I. Dixon, S. Kim, K. R. Bhattachari, S. Noguchi, J. Jaroszynski *et al.*, "45.5-tesla direct-current magnetic field generated with a high-temperature superconducting magnet," *Nature*, vol. 570, no. 7762, pp. 496–499, 2019.
- [35] L. Ren, S. Guo, G. Chen, L. Su, Y. Xu, J. Shi, and L. Chen, "Experimental research on critical current behavior of various commercial hts tapes," *IEEE Trans. Appl. Supercond.*, vol. 30, no. 4, p. 6601006, 2020.
- [36] S. Zhang, K. Xu, and T. Jow, "The low temperature performance of li-ion batteries," *J. Power Sources*, vol. 115, no. 1, pp. 137–140, 2003.
- [37] A. Argon, "A theory for the low-temperature plastic deformation of glassy polymers," *Philos. Mag. Lett.*, vol. 28, no. 4, pp. 839–865, 1973.
- [38] A. Ruiz-Aguirre, J. A. Andrés-Mañas, and G. Zaragoza, "Evaluation of permeate quality in pilot scale membrane distillation systems," *Membranes*, vol. 9, no. 6, p. 69, 2019.
- [39] "Skin friction drag," <https://en.wikipedia.org/wiki/Skin>, feb 1 2017.
- [40] J. Isdale, C. Spence, and J. Tudhope, "Physical properties of sea water solutions: viscosity," *Desalination*, vol. 10, no. 4, pp. 319–328, 1972.
- [41] I. Cheeseman, "Fluid-dynamic drag: Practical information on aerodynamic drag and hydrodynamic resistance. sf hoerner. hoerner fluid dynamics, brick town, new jersey. 1965," *Aeronaut. J.*, vol. 80, no. 788, 1976.
- [42] S. C. Wimbush, "Robinson HTS Wire Critical Current Database," <https://htsdb.wimbush.eu/>.
- [43] Y. Iwasa, *Case Studies in Superconducting Magnets: Design and Operational Issues*, apr 5 2009.
- [44] Y. Li, T. Qu, M. Wu, N. Hu, F. Feng, C. Gu, and Z. Han, "Stress Reduction and Storage Capacity Enhancement of the HTS-SMES Using Reinforcing Overbanding Structure," *IEEE Transactions on Applied Superconductivity*, vol. 27, no. 4, pp. 1–5, 6 2017.
- [45] J. Park, J. Bang, U. Bong, J. Kim, D. Abraimov, and S. Hahn, "Parametric Study on Effect of Friction and Overbanding in Screening Current Stress of LBC Magnet," *IEEE Transactions on Applied Superconductivity*, vol. 31, no. 5, pp. 1–5, 8 2021.
- [46] T. Ando and T. Shakouchi, "Flow characteristics over forward facing step and through abrupt contraction pipe and drag reduction," *Res. Rep. Fac. Eng. Mie Univ.*, vol. 29, pp. 1–8, 2004.
- [47] X. Wang, A. B. Yahia, E. Bosque, P. Ferracin, S. Gourlay, R. Gupta, H. Higley, V. Kashikhin, M. Kumar, V. Lombardo, M. Marchevsky, R. Teyber, and S. Viarengo, "Rebco – a silver bullet for our next high-field magnet and collider budget?" 2022.
- [48] A. Molodyk and D. C. Larbalestier, "The prospects of high-temperature superconductors," *Science*, vol. 380, no. 6651, pp. 1220–1222, 2023.
- [49] Z. S. Hartwig, R. F. Vieira, D. Dunn, T. Golfinopoulos, B. LaBombard, C. J. Lammi, P. C. Michael, S. Agabian, D. Arsenault, R. Barnett *et al.*, "The sparc toroidal field model coil program," *IEEE Transactions on Applied Superconductivity*, 2023.